INTERNATIONAL JOURNAL FOR NUMERICAL METHODS IN ENGINEERING
Int. J. Numer. Meth. Engng (2008)
Published online in Wiley InterScience (www.interscience.wiley.com). DOI: 10.1002/nme.2294

The fractal finite element method for added-mass-type problems

A. Y. T. Leung[1], A. S. L. Fok[2,*,†], H. Dai[2] and R. K. L. Su[3]

[1]*Department of Building and Construction, City University of Hong Kong, Tat Chee Avenue, Kowloon, Hong Kong, China*
[2]*School of Mechanical, Aerospace and Civil Engineering, The University of Manchester, Sackville Street, Manchester M60 1QD, U.K.*
[3]*Department of Civil Engineering, The University of Hong Kong, Pokfulam Road, Hong Kong, China*

SUMMARY

The fractal finite element method (FFEM), originally developed for calculating stress intensity factors in fracture mechanics problems, has been extended to analyse fluid–structure interaction in the form of added-mass-type problems. These include the free vibration of a submerged spherical shell and the interaction between a dam and a reservoir. For the former problem, the numerical solution from the FFEM agrees well with the analytical solution, and the FFEM performed better than conventional finite elements and infinite elements in terms of efficiency. For the latter problem, the FFEM predicted an added mass profile that is different from that based on Westergaard's parabolic solution. Copyright © 2008 John Wiley & Sons, Ltd.

Received 15 August 2006; Revised 29 November 2007; Accepted 5 December 2007

KEY WORDS: fractal finite element; unbounded problems; fluid–structure interaction; added mass

1. INTRODUCTION

In this paper, fluid–structure interaction problems are analysed using the fractal finite element method (FFEM). Specifically, the method is applied to the problem of harmonic vibration of fluid–structure-coupled systems wit an unbounded fluid domain.

There are many problems that involve the combined motion of a fluid and a structure. Examples of such problems include the response of a dam and reservoir to an earthquake, the response of

*Correspondence to: A. S. L. Fok, School of Mechanical, Aerospace and Civil Engineering, University of Manchester, Sackville Street, Manchester M60 1QD, U.K.
†E-mail: alex.fok@manchester.ac.uk

Contract/grant sponsor: Hong Kong Research Grants Council
Contract/grant sponsor: Hong Kong University

ships and other vessels to waves, and the motion of a launcher rocket with a liquid fuel. Zienkiewicz and Taylor [1] gives the following description of such problems: 'Frequently two or more physical systems interact with each other, with the independent solution of any one system being impossible without simultaneous solution of the others. Such systems are known as coupled and of course such coupling may be weak or strong depending on the degree of interaction.' Here, neither the fluid nor the structural system can be solved independently of the other due to the unknown forces at the interface.

The inertia effect of the surrounding fluid medium on the dynamic characteristics, such as natural frequencies, of immersed structures can be significant. This is especially true of structures having large areas of contact with the surrounding fluid, such as plates and shells. The study of the vibration of immersed plate and shell structures has therefore received much attention. For example, the vibration of infinitely long cylindrical shells in an acoustic medium has been analysed by Junger and Mass [2] and Bleich and Baron [3], etc. while that of a spherical shell has been considered by Hayek [4]. In ocean engineering, the vibration of a ship in water is often considered to be equivalent to that of a ship with an additional mass or 'added mass' in the vacuum. Such added-mass-type problems have been investigated numerically by Nicolas-Vullierme and Blumstein [5], Nicolas-Vullierme and Ohayon [6] and Orsero and Armand [7, 8], etc. In these works, the eigenfrequencies of the structure for the conservative system were computed using infinite elements to model the unbounded fluid domain. More recent references on ship vibration problems can be found in Ozsoysal's review [9]; and for those in relation to slamming and whipping of fast and conventional ships in particular, one can refer to References [10, 11].

In a very considerable range of problems, the fluid displacement remains small while the interaction is substantial. In such cases, the simplest approach for taking account of the flow around a vibrating structure is the potential flow idealization. This means that the surrounding fluid is assumed to be incompressible and non-viscous, and its flow is assumed to be irrotational. The equations of the fluid then simply reduce to Laplace's equation in terms of the fluid pressure, allowing the FFEM developed for static problems [12] to be directly applicable to such dynamic problems.

The fluid and structure can be discretized in many different ways, one of which is to discretize the solid using conventional finite elements with the displacements as unknowns, and to discretize the fluid using finite elements with the pressure as unknown. With the FFEM, a mesh with an infinite number of layers of self-similar elements will be generated in the unbounded fluid domain, but only the element matrices of the first layer need to be calculated since the matrices of self-similar elements are related in a simple manner via the similarity or proportional constant. The global interpolating functions, in the form of a truncated infinite series, can then be employed to transform the infinite number of nodal variables to a small number of unknown coefficients associated with the global interpolating functions. The fluid field can then be described completely by the nodal pressures at the interface plus a small set of unknown coefficients. Because of this and the fact that only conventional finite elements are required, for the same degree of solution accuracy, the computational expense associated with the FFEM is small compared with other methods, e.g. the use of either a truncated mesh with conventional finite elements or infinite elements.

The FFEM has proved to be an economic, accurate and easy-to-implement method to impose boundary conditions in the far field, whereby good approximation of the near-field behaviour of the system can be obtained [12]. In this paper, the method is used for the free vibration analysis of an elastic spherical shell immersed in an incompressible fluid and that of a

DOI: 10.1002/nme

dam–reservoir structure. Accurate frequency results have been obtained as shown in the numerical examples.

2. THEORY

2.1. Fluid behaviour

Consider the small oscillations of a structure immersed in a fluid domain extending to infinity in all directions (Figure 1). The fluid is assumed to be incompressible as well as being inviscid. Its behaviour is described by a simple Laplace's equation of the form

$$\nabla^2 p = 0 \tag{1}$$

where p is the pressure above the hydrostatic value.

At the interface, S_h, with the solid, Euler's equation must be satisfied, i.e.

$$\frac{\partial p}{\partial \mathbf{n}} = -\rho_{\mathrm{f}} \ddot{u}_n \tag{2}$$

where u_n is the displacement normal to the interface, ρ_f is the density of the fluid and $\mathbf{n}$ is the direction cosine vector for an inward pointing normal to the structure.

At the boundary, S_∞, at infinity, the boundary condition is

$$p = 0 \quad \text{on} \quad S_\infty \tag{3}$$

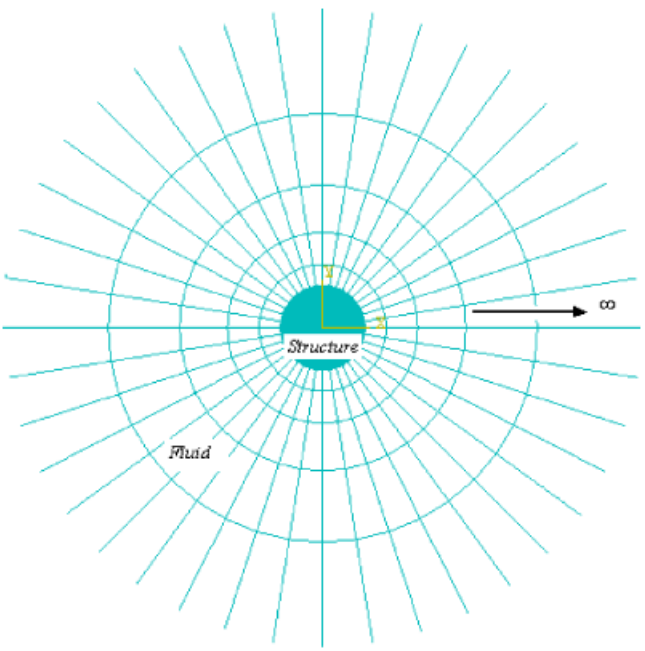

Figure 1. Structure immersed in an infinite fluid domain with interface S_h.

DOI: 10.1002/nme

In spherical coordinates, where

$$x = r\sin\theta\cos\phi \tag{4}$$

$$y = r\sin\theta\sin\phi \tag{5}$$

$$z = r\cos\theta \tag{6}$$

Equation (1) has the form

$$\frac{1}{r^2\sin\theta}\left(\frac{\partial}{\partial r}\left(r^2\sin\theta\frac{\partial p}{\partial r}\right)+\frac{\partial}{\partial\theta}\left(\sin\theta\frac{\partial p}{\partial\theta}\right)+\frac{\partial}{\partial\phi}\left(\frac{1}{\sin\theta}\frac{\partial p}{\partial\phi}\right)\right)=0 \tag{7}$$

According to [13], the general solution of Equation (7) is

$$p(r,\theta,\phi)=\sum_{n=0}^{\infty}\sum_{m=0}^{n} r^{-(n+1)}P_n^m(\cos\theta)\{A_{nm}\cos(m\phi)+B_{nm}\sin(m\phi)\} \tag{8}$$

where $P_n^m(\cos\theta)$ are Legendre functions. For axisymmetric problems, the solution reduces to

$$p(r,\theta)=\sum_{n=0}^{\infty} r^{-(n+1)}P_n(\cos\theta)A_n \tag{9}$$

It should be noted that this solution is an infinite decay series which, for computational purposes, can be truncated into a finite number of terms with M unknowns or generalized coordinates, i.e. A_n $(n=0,1,\ldots,M-1)$. A truncated series of Equation (9) will therefore be used as the global interpolation function in the FFEM to transform the nodal pressures in the far field into a set of generalized coordinates. M is thus called the number of transformation terms.

2.2. Discretization of the coupled fluid–structure systems

The coupled problem can be discretized in the standard manner with the displacement vector approximated as

$$\mathbf{u}\approx\mathbf{N_u}\tilde{\mathbf{u}} \tag{10}$$

and the fluid pressure as

$$p\approx\mathbf{N_p}\tilde{\mathbf{p}} \tag{11}$$

where $\mathbf{N_u}$ and $\mathbf{N_p}$ are interpolation functions, $\mathbf{u}$ is the displacement vector for the structure, p is the pressure in the fluid domain, $\tilde{\mathbf{u}}$ are the nodal displacements in the structure, and $\tilde{\mathbf{p}}$ are the nodal pressures in the fluid domain.

According to Zienkiewicz and Taylor [1], the governing equations for the free vibration of the coupled system are

$$\begin{bmatrix}\mathbf{M} & \mathbf{0}\\ \rho_f\mathbf{Q}^T & \mathbf{0}\end{bmatrix}\begin{Bmatrix}\ddot{\tilde{\mathbf{u}}}\\ \ddot{\tilde{\mathbf{p}}}\end{Bmatrix}+\begin{bmatrix}\mathbf{K} & -\mathbf{Q}\\ \mathbf{0} & \mathbf{H}\end{bmatrix}\begin{Bmatrix}\tilde{\mathbf{u}}\\ \tilde{\mathbf{p}}\end{Bmatrix}=0 \tag{12}$$

DOI: 10.1002/nme

where **M** and **K** are the mass and stiffness matrices of the structure, respectively, **H** is the matrix derived from Laplace's equation for the fluid domain:

$$\mathbf{H}=\int_{\Omega}(\nabla\mathbf{N_p})^{\mathrm{T}}\nabla\mathbf{N_p}\,\mathrm{d}\Omega \tag{13}$$

ρ_{f} is the density of the fluid and **Q** is the matrix due to fluid–structure interaction:

$$\mathbf{Q}=\int_{S_h}\mathbf{N}_{\mathbf{u}}^{\mathrm{T}}\mathbf{n}\mathbf{N_p}\,\mathrm{d}S \tag{14}$$

By putting $\tilde{\mathbf{u}}=\breve{\mathbf{u}}\,\mathrm{e}^{\mathrm{i}\omega t}$ and $\tilde{\mathbf{p}}=\breve{\mathbf{p}}\,\mathrm{e}^{\mathrm{i}\omega t}$, Equation (12) can be rewritten as

$$(\mathbf{K}-\omega^2\mathbf{M})\breve{\mathbf{u}}-\mathbf{Q}\breve{\mathbf{p}}=0 \tag{15}$$

and

$$\mathbf{H}\breve{\mathbf{p}}-\rho_{\mathrm{f}}\omega^2\mathbf{Q}^{\mathrm{T}}\breve{\mathbf{u}}=0 \tag{16}$$

2.3. The FFEM

When using the FFEM to analyse the coupled system, the fluid region is discretized into layers of self-similar or fractal elements with increasing dimensions; as shown in Figure 1. Each layer is created from the adjacent inner layer using the same proportional constant or similarity ratio. The infinite number of nodal pressures will be transformed into a finite set of generalized coordinates using the global interpolation functions derived from (9). Similar to the stiffness matrices [12], it can be shown that there is a simple relation between the **H** matrices of similar elements, which allows this transformation to be performed at the local element level and the results summed up as geometrical progression series to be assembled to the global **H** matrix (see later). The contributions to the global **H** matrix from the infinite number of elements in the unbounded domain are therefore fully accounted for, while the number of degrees of freedom remains finite.

Following procedures similar to those for static problems [12], the fluid matrix equation, (16), for the first layer is partitioned with respect to the slave nodes (r) in the fluid region and the master nodes (h) at the fluid–structure interface:

$$\begin{bmatrix}\mathbf{H}_{hh} & \mathbf{H}_{hr}\\ \mathbf{H}_{rh} & \mathbf{H}_{rr}\end{bmatrix}\begin{Bmatrix}\breve{\mathbf{P}}_h\\ \breve{\mathbf{P}}_r\end{Bmatrix}=\begin{Bmatrix}\rho_{\mathrm{f}}\omega^2\mathbf{Q}^{\mathrm{T}}\breve{\mathbf{u}}_h\\ 0\end{Bmatrix} \tag{17}$$

Using the transformation

$$\breve{\mathbf{p}}_r=\mathbf{T}_r\mathbf{a}$$

where $\mathbf{T}_r$ is the transformation matrix evaluated from the truncated series of Equation (9) and **a** are the associated generalized coordinates, the pressure vector can be expressed as

$$\begin{Bmatrix}\breve{\mathbf{p}}_h\\ \breve{\mathbf{p}}_r\end{Bmatrix}=\begin{bmatrix}\mathbf{I} & 0\\ 0 & \mathbf{T}_r\end{bmatrix}\begin{Bmatrix}\breve{\mathbf{p}}_h\\ \mathbf{a}\end{Bmatrix} \tag{18}$$

DOI: 10.1002/nme

Substituting Equation (18) into Equation (17) yields

$$\begin{bmatrix} \mathbf{H}_{hh} & \mathbf{H}_{hr}\mathbf{T}_r \\ \mathbf{H}_{rh} & \mathbf{H}_{rr}\mathbf{T}_r \end{bmatrix} \begin{Bmatrix} \breve{\mathbf{P}}_h \\ \mathbf{a} \end{Bmatrix} = \begin{Bmatrix} \rho_{\mathrm{f}}\omega^2\mathbf{Q}^{\mathrm{T}}\breve{\mathbf{u}}_h \\ 0 \end{Bmatrix} \tag{19}$$

Pre-multiplying the equation by the transpose of the transformation matrix, i.e.

$$\begin{bmatrix} \mathbf{I} & 0 \\ 0 & \mathbf{T}_r \end{bmatrix}^{\mathrm{T}}$$

on both sides then gives

$$\begin{bmatrix} \mathbf{H}_{hh} & \mathbf{H}_{hr}\mathbf{T}_r \\ \mathbf{T}_r^{\mathrm{T}}\mathbf{H}_{rh} & \mathbf{T}_r^{\mathrm{T}}\mathbf{H}_{rr}\mathbf{T}_r \end{bmatrix} \begin{Bmatrix} \breve{\mathbf{P}}_h \\ \mathbf{a} \end{Bmatrix} = \begin{Bmatrix} \rho_{\mathrm{f}}\omega^2\mathbf{Q}^{\mathrm{T}}\breve{\mathbf{u}}_h \\ 0 \end{Bmatrix} \tag{20}$$

Similarly, for the second and subsequent layers in the unbounded fluid domain, i.e. $k \geqslant 2$, we have

$$\mathbf{T}_k^{\mathrm{T}}\mathbf{H}_k\mathbf{T}_k\mathbf{a} = 0 \tag{21}$$

By summing the contributions from all fluid layers, i.e. adding Equations (21) for all k to Equation (20), Equation (16) can be expressed as

$$\begin{bmatrix} \mathbf{H}_{hh} & \mathbf{H}_{hr}\mathbf{T}_r \\ \mathbf{T}_r^{\mathrm{T}}\mathbf{H}_{rh} & \mathbf{T}_r^{\mathrm{T}}\mathbf{H}_{rr}\mathbf{T}_r + \sum_{k=2}^{\infty}\mathbf{T}_k^{\mathrm{T}}\mathbf{H}_k\mathbf{T}_k \end{bmatrix} \begin{Bmatrix} \breve{\mathbf{P}}_h \\ \mathbf{a} \end{Bmatrix} = \begin{Bmatrix} \rho_{\mathrm{f}}\omega^2\mathbf{Q}^{\mathrm{T}}\breve{\mathbf{u}}_h \\ 0 \end{Bmatrix} \tag{22}$$

From the lower part of Equation (22) above, we have

$$\mathbf{a} = -\mathbf{L}^{-1}\mathbf{T}_r^{\mathrm{T}}\mathbf{H}_{rh}\breve{\mathbf{p}}_h \tag{23}$$

where

$$\mathbf{L} = \left(\mathbf{T}_r^{\mathrm{T}}\mathbf{H}_{rr}\mathbf{T}_r + \sum_{k=2}^{\infty}\mathbf{T}_k^{\mathrm{T}}\mathbf{H}_k\mathbf{T}_k\right) \tag{24}$$

Substituting this back into the upper part of Equation (22) yields

$$\breve{\mathbf{P}}_h = \rho_{\mathrm{f}}\omega^2\mathbf{H}_A^{-1}\mathbf{Q}^{\mathrm{T}}\breve{\mathbf{u}}_h \tag{25}$$

where

$$\mathbf{H}_A = \mathbf{H}_{hh} - \mathbf{H}_{hr}\mathbf{T}_r\mathbf{L}^{-1}\mathbf{T}_r^{\mathrm{T}}\mathbf{H}_{rh} \tag{26}$$

Finally, substituting Equation (25) into Equation (15) gives the equation for the free vibration of the coupled system:

$$[\mathbf{K} - \omega^2(\mathbf{M}_\alpha + \mathbf{M})]\breve{\mathbf{u}} = 0 \tag{27}$$

where the added mass is given by

$$\mathbf{M}_\alpha = \rho_f\mathbf{Q}\mathbf{H}_A^{-1}\mathbf{Q}^{\mathrm{T}} \tag{28}$$

DOI: 10.1002/nme

To solve Equation (27), one must first calculate the summation

$$\sum_{k=2}^{\infty} \mathbf{T}_k^{\mathrm{T}} \mathbf{H}_k \mathbf{T}_k$$

To this end, consider two axisymmetric elements, denoted by a and b, which are similar in the r direction with α being the proportional constant. It follows from (4) to (6) that the nodal coordinates in element b can be expressed in terms of these in element a via

$$\mathbf{X}_b = \alpha \mathbf{X}_a$$

It can then be shown that

$$\nabla \mathbf{N}_p^b = \frac{1}{\alpha} \nabla \mathbf{N}_p^a$$

and

$$\mathrm{d}\Omega_b = 2\pi X_b \, \mathrm{d}S_b = \alpha^3 \cdot 2\pi X_a \, \mathrm{d}S_a = \alpha^3 \cdot \mathrm{d}\Omega_a$$

where $\mathbf{N}_p^a$ and $\mathbf{N}_p^b$ are interpolation functions, Ω_a and Ω_b are volumes, and S_a and S_b are areas of elements a and b, respectively. For axisymmetric elements, therefore, the $\mathbf{H}$ matrix, Equation (13), of element b is related to that of element a via

$$\mathbf{H}_b = \int_{\Omega_b} (\nabla \mathbf{N}_p^b)^{\mathrm{T}} \nabla \mathbf{N}_p^b \, \mathrm{d}\Omega = \alpha \mathbf{H}_a \tag{29}$$

It follows by induction that

$$\mathbf{H}_k = \alpha^{k-2} \mathbf{H}_2 \tag{30}$$

From (9), it can be seen that

$$\mathbf{T}_k = \mathbf{T}_2 \mathbf{Diag}[\alpha_i] \tag{31}$$

where

$$\alpha_i = \alpha^{-(k-2)i} \tag{32}$$

is a scaling function and $i = 1, 2, 3 \ldots M$.

Thus,

$$\sum_{k=2}^{\infty} \mathbf{T}_k^{\mathrm{T}} \mathbf{H}_k \mathbf{T}_k = \sum_{k=2}^{\infty} \alpha^{(k-2)} \cdot \mathbf{Diag}[\alpha_i]^{\mathrm{T}} \mathbf{T}_2^{\mathrm{T}} \mathbf{H}_2 \mathbf{T}_2 \mathbf{Diag}[\alpha_j] = [\overline{\alpha}_{ij} \overline{H}_{ij}] \tag{33}$$

where

$$\overline{\alpha}_{ij} = \sum_{k=2}^{\infty} \alpha^{-(k-2)i} \cdot \alpha^{(k-2)} \cdot \alpha^{-(k-2)j} = [1 - \alpha^{-(i+j-1)}]^{-1} \tag{34}$$

and

$$[\overline{H}_{ij}] = \mathbf{T}_2^{\mathrm{T}} \mathbf{H}_2 \mathbf{T}_2 \tag{35}$$

with $i, j = 1, 2, \ldots, M$.

The FFEM has been coded and used to solve some added-mass-type problems. The followings present the numerical calculations conducted to verify the program.

DOI: 10.1002/nme

3. APPLICATION

3.1. Free vibration analysis of a spherical shell immersed in an incompressible fluid

The geometrical dimensions and mechanical properties used in this problem are shell radius $r_0 = 2.5\,\text{m}$, shell thickness $h = 0.01\,\text{m}$, shell density $\rho_s = 7800\,\text{kg/m}^3$, fluid density $\rho_f = 1000\,\text{kg/m}^3$, Young's modulus of shell $E = 2 \times 10^{11}\,\text{N/m}^2$, and its Poisson ratio $v = 0.3$. The analytical solution to this problem can be found in [4, 6].

3.1.1. FFEM vs FEM with a truncated fluid domain. For this problem, the spherical shell was modelled using 300 axisymmetric shell elements (SAX1) [14], giving 903 degrees of freedom (DOF) for the structure. The fluid domain was modelled using acoustic elements (ACAX4) [11], no infinite elements being used in this case. As a minimum, a truncated fluid domain with only one layer of acoustic elements may be used, for which the number of DOF would be 1204. However, to obtain reasonably accurate results without using infinite elements or the fractal element method, more layers of acoustic elements were required. For this example, 10 layers of acoustic elements were used, with the fluid domain being truncated at a radius $r = 5\,\text{m}$. The total number of DOF was 7525. Figure 2 shows some of the modes of vibration predicted by the model using finite elements only.

The FFEM, on the other hand, could provide equally accurate results with much fewer DOF. In this case, the number of transformation terms used was 12 and the similarity ratio was 1.10. The number of DOF of the FFE model was 915. Table I compares the FFE results with both the analytical solution [4, 6] and the results from the model with a truncated domain of finite elements only. As can be seen, the three sets of results agree well with each other. However, the higher efficiency of the FFEM is clearly illustrated by the fact that the number of DOF in the FFE model was only 1/8th of that in the finite element model.

3.1.2. Convergence of FFE results. Table II shows the changes of the FFE frequency results with increasing number of transformation terms, M. The similarity ratio used was kept at 1.10. As can be seen, the results for a particular frequency take the form of a step change at a particular M value; the higher the frequency, the higher the M value at which the step change takes place. Although no other step changes are apparent with further increase of M, such behaviour is not typical of numerical convergence.

To ensure that convergence of the numerical results had truly been achieved, and to understand the step change behaviour of the frequency results, the convergence with increasing M of the added mass values associated with different nodes on the spherical shell were investigated. The added mass of five nodes on the top half of the axisymmetric shell model (Figure 2) and their convergence with increasing M are given in Table III. Their normalized values, using those for $M = 20$, are plotted in Figure 3 to further illustrate the rate of convergence with increasing M. All the nodal added mass values presented converge to within 2% for $M \geqslant 5$. Note that, due to symmetry, the corresponding nodes on the bottom half of the shell will have the same added mass values. Note also that the added mass is independent of the mode shape and frequency.

As can be seen from Table III and Figure 3, the nodes at the poles have much smaller added mass and the rate of convergence with increasing M is slower than that of the node at the equator. Therefore, for the lower modes of vibration, which will be dominated by the motion of the nodes close to the equator, due to their much larger added mass, the convergence of the numerical results

DOI: 10.1002/nme

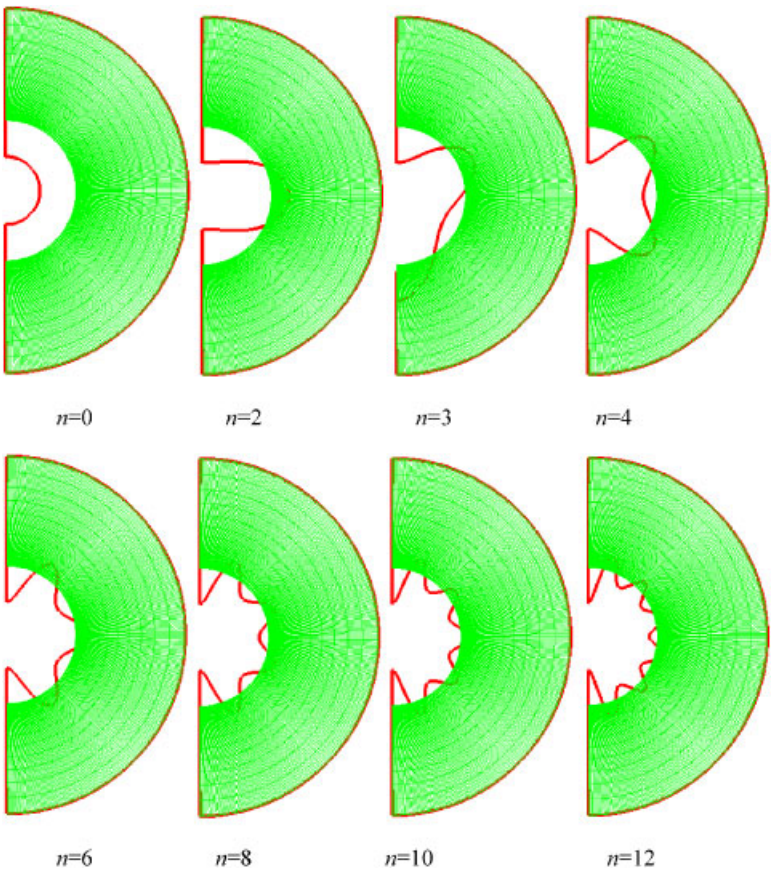

Figure 2. Modes of free vibration of the submerged spherical shell (n is mode number).

Table I. Predicted natural frequencies for spherical shell immersed in incompressible fluid (for FFEM, similarity ratio $\alpha = 1.10$, number of transformation terms $M = 12$).

n	Analytical	FFEM	FEM
2	80.68	80.94	78.93
0	94.77	94.92	94.30
3	100.14	100.61	98.20
4	113.70	114.42	112.27
5	124.63	125.67	123.79
6	133.93	135.37	133.69
8	149.72	151.95	150.50
10	163.06	166.31	164.95
11	175.17	173.03	171.68

DOI: 10.1002/nme

Table II. Convergence of the FFE frequency results for submerged spherical shell with increasing number of transformation terms M (similarity ratio $\alpha = 1.10$, '—' signifies identical results as per lower M values).

n	$M=4$	$M=5$	$M=6$	$M=7$	$M=8$	$M=9$	$M=10$	$M=12$	$M=20$
2	80.94	—	—	—	—	—	—	—	—
0	94.92	—	—	—	—	—	—	—	—
3	100.61	—	—	—	—	—	—	—	—
4	159.08	114.42	—	—	—	—	—	—	—
5	163.40	163.40	125.66	—	—	—	—	—	—
6	169.20	169.20	169.20	133.37	—	—	—	—	—
7	170.22	170.22	170.22	170.22	144.04	—	—	—	—
8	173.54	173.54	173.54	173.54	173.54	151.95	—	—	—
9	177.01	177.01	177.01	177.01	177.01	177.01	159.33	—	—
10	180.69	180.69	180.69	180.69	180.69	180.69	180.69	166.31	166.31
11	184.63	184.63	184.63	184.63	184.63	184.63	184.63	173.03	173.03

Table III. Convergence of nodal added mass M_a (kg) against the number of transformation terms M.

M_a / M	$\theta=0$	$\theta=0.12\pi$	$\theta=0.25\pi$	$\theta=0.38\pi$	$\theta=0.5\pi$
1	1.125E−01	2.486E+01	4.807E+01	6.427E+01	6.989E+01
2	1.339E−01	2.956E+01	5.414E+01	6.683E+01	6.989E+01
3	1.328E−01	2.945E+01	5.328E+01	7.004E+01	7.763E+01
4	1.323E−01	2.933E+01	5.392E+01	7.258E+01	7.763E+01
5	1.312E−01	2.915E+01	5.517E+01	7.261E+01	7.906E+01
6	1.305E−01	2.908E+01	5.571E+01	7.328E+01	7.906E+01
7	1.300E−01	2.911E+01	5.575E+01	7.360E+01	7.970E+01
8	1.296E−01	2.918E+01	5.581E+01	7.362E+01	7.970E+01
9	1.294E−01	2.928E+01	5.597E+01	7.388E+01	7.996E+01
10	1.293E−01	2.935E+01	5.607E+01	7.392E+01	7.996E+01
11	1.292E−01	2.940E+01	5.608E+01	7.396E+01	8.009E+01
12	1.291E−01	2.943E+01	5.609E+01	7.403E+01	8.009E+01
13	1.291E−01	2.943E+01	5.613E+01	7.404E+01	8.014E+01
14	1.291E−01	2.943E+01	5.615E+01	7.406E+01	8.014E+01
15	1.291E−01	2.943E+01	5.615E+01	7.408E+01	8.017E+01

with increasing M is expected to be faster. In contrast, the higher modes is expected to have a slower rate of convergence since the poles will have a bigger contribution to the motion, as indicated by the mode shapes shown in Figure 2.

We are now in a position to explain the step change behaviour of the frequency results shown in Table II. Given that the frequency of free vibration is inversely proportional to the square root of mass, the convergence with increasing M of the natural frequencies of the immersed shell is expected to mirror that of the inverse of the square root of the total added mass. However, before summing them up, the nodal added mass values (m_{a_i}) need to be weighted by the eigenvector (v_i) for a particular mode of vibration, for different nodes will have different contributions to the motion, as explained above. Figure 4 shows the changes with increasing M of $1/\sqrt{\sum m_{a_i} v_i}$ for several modes of vibration. The step changes in the results, which are very similar to those in the frequencies, can clearly be seen. Thus, the results presented in Table II for the natural frequencies

DOI: 10.1002/nme

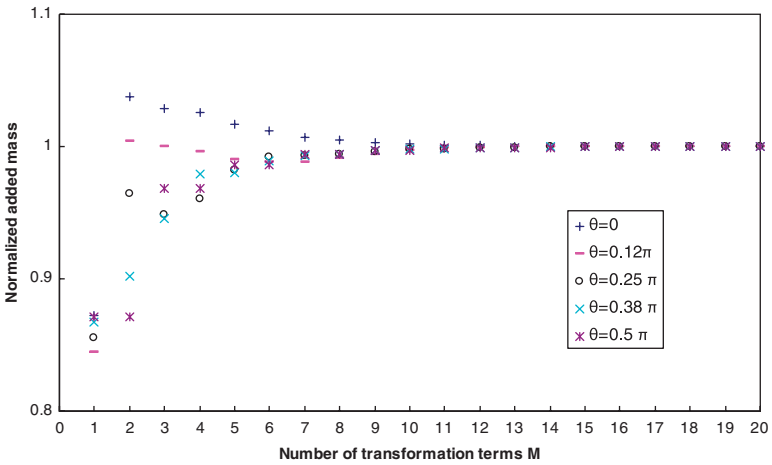

Figure 3. Normalized added mass for five shell nodes against transformation terms M.

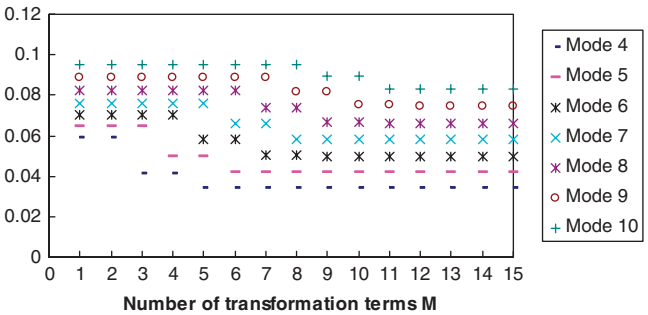

Figure 4. $1/\sqrt{\sum m a_i v_i}$ against the number of transformation terms M.

can be considered as demonstration of their convergence with the number of transformation terms M.

Figure 5 shows the convergence of the FFE results with the similarity ratio. As found for static problems [12, 15], the closer to unity is the similarity ratio, i.e. the larger the number of fractal elements used per unit distance in the unbounded domain, the more accurate is the solution. For example, for mode 10, the frequency converges from within 50% to within 3% of the analytical solution when the similarity ratio changes from 2.0 to 1.1. Since the value of the similarity ratio does not affect the size of the problem, a value close to unity is recommended for generating the fractal mesh. However, as will be seen later, this only applies to problems where a closed-form solution is available for the summation of the infinite transformed matrices.

3.1.3. Comparison with infinite elements. The FFE results will now be compared with those of Nicolas-Vullierme and Ohayon [6] who applied a combination of finite and infinite elements to

DOI: 10.1002/nme

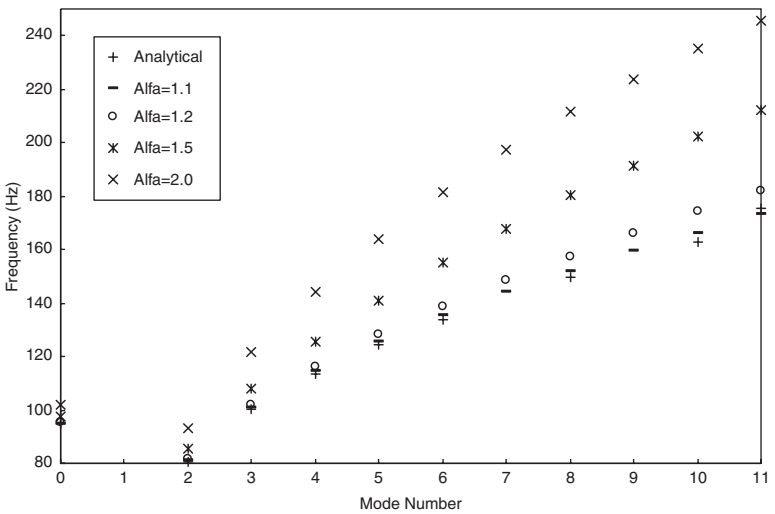

Figure 5. Convergence of the FFE frequency results for submerged spherical shell with changing similarity ratios α (number of transformation terms $M=12$).

Table IV. Frequency results for submerged spherical shell: comparison between FFE and infinite elements [7] (for FFEM, $\alpha=1.10$, number of transformation terms $M=12$).

n	Analytical	FFEM	First mesh	Second mesh	Third mesh	Fourth mesh
2	80.68	80.94	81.30	83.20	82.13	81.28
0	94.77	94.92	102.39	132.46	94.99	112.10
3	100.14	100.61	101.34			
4	113.70	114.42	116.70	113.70	113.10	112.10
5	124.63	125.66				
6	133.93	135.37	138.08	137.90	137.90	137.80
8	149.72	151.95			154.37	
10	163.06	166.31			170.11	
11	175.17	173.03			181.10	

the problem. Four different computations with spherical boundaries of different radii r were used by these workers:

1. Truncation of fluid domain at $r=7r_0$, finite element mesh.
2. Truncation of fluid domain at $r=2r_0$, finite element mesh.
3. Intermediary boundary at $r=2r_0$, finite elements inside, infinite $1/r$ type elements outside.
4. Intermediary boundary at $r=2r_0$, finite elements inside, infinite $1/r^3$ type elements outside.

There was no information on the order of the elements and the mesh density used.

Table IV compares the results from the FFEM with the analytical solution and those from Reference [6] (denoted as first, second, third and fourth mesh). In general, the FFE results are closer to the analytical solution than those given in [6].

DOI: 10.1002/nme

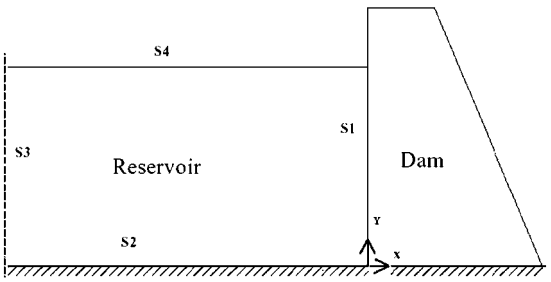

Figure 6. Dam and reservoir with rigid bottom.

3.2. *Free vibration analysis of a concrete gravity dam*

3.2.1. Global interpolation functions. To model dam–reservoir interaction, a 2-D model of a gravity dam (Figure 6) was adopted. Assuming water to be incompressible, inviscid and irrotational, the hydrostatic pressure, p, in excess of the static pressure due to small-amplitude motion of water is governed by the Laplace equation (1).

At the dam–reservoir interface (S1), where the normal acceleration is prescribed, the boundary condition is given by Euler's equation (2). Neglecting the effects of surface waves, the boundary condition at the free surface (S4) is $p=0$. This is justified because, even at the lowest frequency (~ 3 Hz, see later), the wavelength of the surface waves is less than 0.3 m, which is much smaller than the characteristic dimensions of the problem. At higher frequencies, the wavelength of the surface waves would be even smaller. The same boundary condition ($p=0$) applies at the far end (S3) where x is infinite. If the bottom of the reservoir is assumed to be rigid, the boundary condition at the bottom of the fluid domain, (S2), may be expressed as

$$\frac{\partial p}{\partial \mathbf{n}} = 0 \tag{36}$$

An analytical solution of Equation (1) satisfying the above given boundary conditions is [16]:

$$p(x, y) = 8a_n \rho_{\mathrm{w}} H \sum_{k=1}^{\infty} \frac{(-1)^{k+1}}{(2k-1)^2 \pi^2} \exp\left(-\frac{(2k-1)\pi x}{2H}\right) \cos\left(\frac{(2k-1)\pi y}{2H}\right) \tag{37}$$

where a_n is the ground acceleration, H is the depth of water, ρ_{w} is the density of water. This equation will be used as the global interpolation function for the FFEM.

3.2.2. Westergaard's added mass. Earthquake-induced hydrodynamic pressures on dams were first investigated by Westergaard mathematically [17]. According to his solution, the hydrodynamic forces exerted on a gravity dam due to earthquake ground motion are equivalent to inertia forces of a volume of water attached to the dam and moving back and forth with the dam, while the rest of the reservoir water remains inactive. For analysis of gravity dams idealized as a 2-D rigid monolith with vertical upstream face, Westergaard proposed a parabolic shape for this body of water. The added mass of water at location i, m_{a_i}, is therefore obtained by multiplying the mass density ρ_{w} of water by the volume of water tributary to point i:

$$m_{\mathrm{a}_i} = \tfrac{7}{8} \rho_{\mathrm{w}} \sqrt{H(H-y_i)} A_i \tag{38}$$

DOI: 10.1002/nme

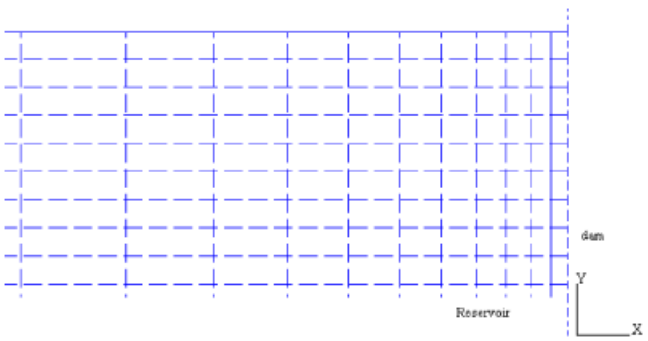

Figure 7. Part of the virtual FFE mesh of the fluid domain ($\alpha = 1.10$ in the x-direction).

where H is the depth of water, y_i the height above the base of the dam, A_i the tributary surface area at point i.

3.2.3. The FFEM. Four-node plane acoustic elements [14] were used for the fluid, part of the mesh being shown in Figure 7. The right-hand side boundary is the interface between the dam and the reservoir. An infinite number of elements were generated in the upstream direction. Each column of elements was created from the adjacent column on the right using the same similarity ratio throughout. The infinite number of nodal pressures was transformed into a finite set of generalized coordinates using the global interpolation functions derived from (37). There is a linear relation between the **H** matrices of similar elements; hence, this transformation could be performed at the local element level and the results summed up as geometrical progression series to be assembled to the global **H** matrix. However, since the fractal principle applies to the x-direction only, the **H** matrix had to be divided into two components. As a result, unlike the previous submerged spherical shell problem, there was no closed-form solution for the summation of the infinite transformed matrices; hence only a finite number of fractal layers could be used for this problem.

From the previous section, the summation to be calculated after fractal transformation is

$$\sum_{n=k}^{\infty} \mathbf{T}_k^{\mathrm{T}} \mathbf{H}_k \mathbf{T}_k$$

The element **H** matrix can be expressed as

$$H_{ij} = \int_{R_e} \left(\frac{\partial N_i}{\partial x} \frac{\partial N_j}{\partial x} + \frac{\partial N_i}{\partial y} \frac{\partial N_j}{\partial y} \right) \mathrm{d}x\, \mathrm{d}y = H_{ij}^x + H_{ij}^y \tag{39}$$

where R_e denotes the region of an element

$$H_{ij}^x = \int_{R_e} \frac{\partial N_i}{\partial x} \frac{\partial N_j}{\partial x} \mathrm{d}x\, \mathrm{d}y \tag{40}$$

and

$$H_{ij}^y = \int_{R_e} \frac{\partial N_i}{\partial y} \frac{\partial N_j}{\partial y} \mathrm{d}x\, \mathrm{d}y \tag{41}$$

DOI: 10.1002/nme

Consider two elements, denoted by a and b, which have the same dimension in the y-direction and are similar in the x-direction with α being the proportional constant, i.e.

$$x_b = \alpha x_a \tag{42}$$

and

$$y_b = y_a \tag{43}$$

It follows that

$$H_b = H_b^x + H_b^y = H_a^x/\alpha + \alpha H_a^y \tag{44}$$

By induction, the components of $\mathbf{H}_k$ $(k \geqslant 2)$ of the outer layers can be derived from those of $\mathbf{H}_2$:

$$H_k = H_k^x + H_k^y = \alpha^{-(k-2)} H_2^x + \alpha^{(k-2)} H_2^y \tag{45}$$

$\mathbf{T}_k$ can be obtained from Equation (37). Note that there is only one transformation term, i.e. a_n.

3.2.4. Numerical computation. A simple 2-D gravity dam model was examined using the FFEM. The geometry of a typical non-overflow monolith of the dam is illustrated in Figure 8. The monolith is 103 m high and 70 m wide at its base. The upstream wall of the monolith is assumed to be straight and vertical, which is slightly different from the real configuration. The depth of the reservoir is $h_w = 91.75$ m. Densities for water and the dam are 1000 and 2643 kg/m^3, respectively, and Young's modulus and the Poisson ratio of the dam concrete are 310.27 GPa and 0.15, respectively. Following the work of other investigators [14, 17], a 2-D analysis of the non-overflow monolith was carried out, assuming plane-stress conditions. The finite element mesh used for the analysis is shown in Figure 9. It consists of 760 first-order, reduced-integration, plane-stress elements (CPS4R [14]).

For simplicity, the dam–foundation interaction was neglected by assuming that the foundation was rigid. The dam–reservoir dynamic interaction resulting from the horizontal component of ground motion was modelled in a simple form using the added mass technique; both Westergaard's added mass formulation and that calculated by the FFEM were used. The FFE approach was implemented in ABAQUS/Standard [14] using a simple 2-node user element that had been coded in its User Element Subroutine UEL. The hydrodynamic pressures resulting from the vertical component of ground motion were assumed to be small and were neglected in all the simulations.

As mentioned previously, no closed-form solution for the summation of sub-**H** matrices in the FFE region exists; hence, 100 layers of FFEs were used with $\alpha = 1.10$. In this case, the value of the similarity ratio and the number of fractal layers must be chosen so as to produce an efficient solution without excessive computational effort. For the interpolation function, (22), 60 terms were used for the summation.

Figure 10 shows the distributed nodal added mass due to the FFE user elements, which is compared with the Westergaard 'added mass'. As can be seen, the FFE predicted added mass profile is quite different from that of Westergaard's, with the former solution giving less added mass in the upper section of the reservoir and more added mass in the lower section. Table V further compares the total mass predicted by Westergaard with that by the FFEM. It can be seen that the FFEM gives slightly higher value for the total added mass. Two of the mode shapes

DOI: 10.1002/nme

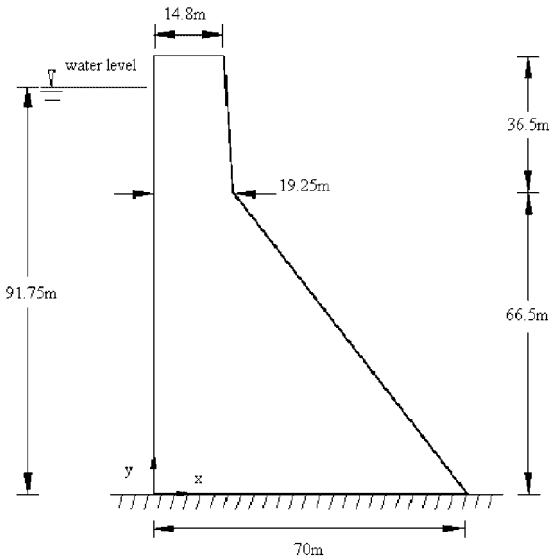

Figure 8. Geometry and dimensions of the dam.

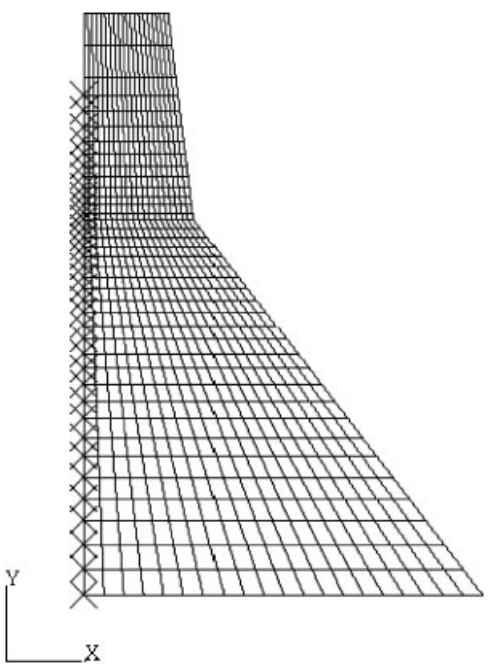

Figure 9. Finite element model for dam, including 2-node user elements for the reservoir.

DOI: 10.1002/nme

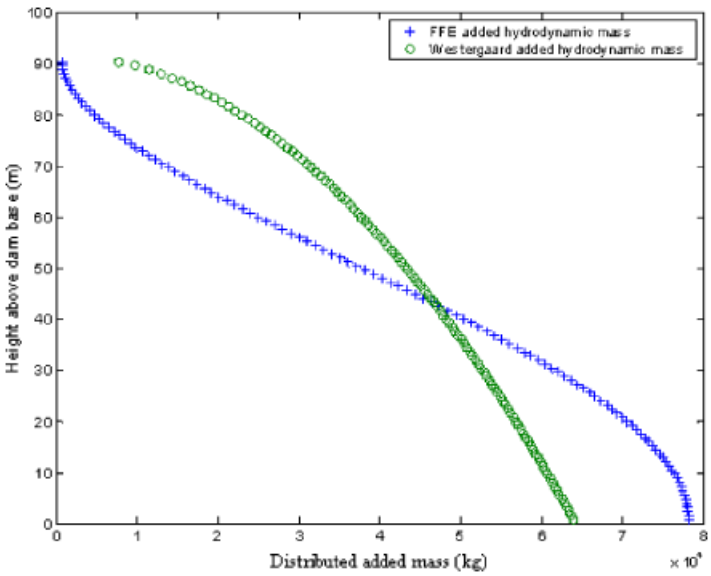

Figure 10. Added mass profiles for dam with full reservoir.

Table V. Total mass of dam with full reservoir.

	Mass associated with direction (kg)		
	x	*y*	*z*
FFEM	1.5046907E+07	9 485 585	0.0
Westergaard	1.4398595E+07	9 485 585	0.0

predicted by the two methods are shown in Figure 11. In Table VI, the natural frequency results due to the two added mass profiles are compared. Not surprisingly, the FFEM predicted slightly lower natural frequencies because of the larger added mass.

Also presented in Table VI are the natural frequencies predicted by ABAQUS using acoustic finite elements (AC2D4) and a truncated boundary to model the reservoir (Figure 12). The distance of truncation ranged from 200 to 800 m. It should be noted that the results for mode 1 with a domain of 200 m will not be very reliable since, given a speed of sound in water of approximately 1500 m/s, mode 1 (2.57 Hz) would have a wavelength of about 580 m. Nevertheless, the ABAQUS results seem to be converging with increasing truncation distance.

There are significant differences between the FFE and ABAQUS frequency results, especially for mode 2 ($\sim$12%). Given that frequency is proportional to the square root of mass, the corresponding discrepancies in the added mass would be even more significant. The discrepancies are attributed to the different formulations of the two methods, with the FFEM being based on potential flow while the ABAQUS acoustic elements being based on compressible fluid. The ABAQUS results

DOI: 10.1002/nme

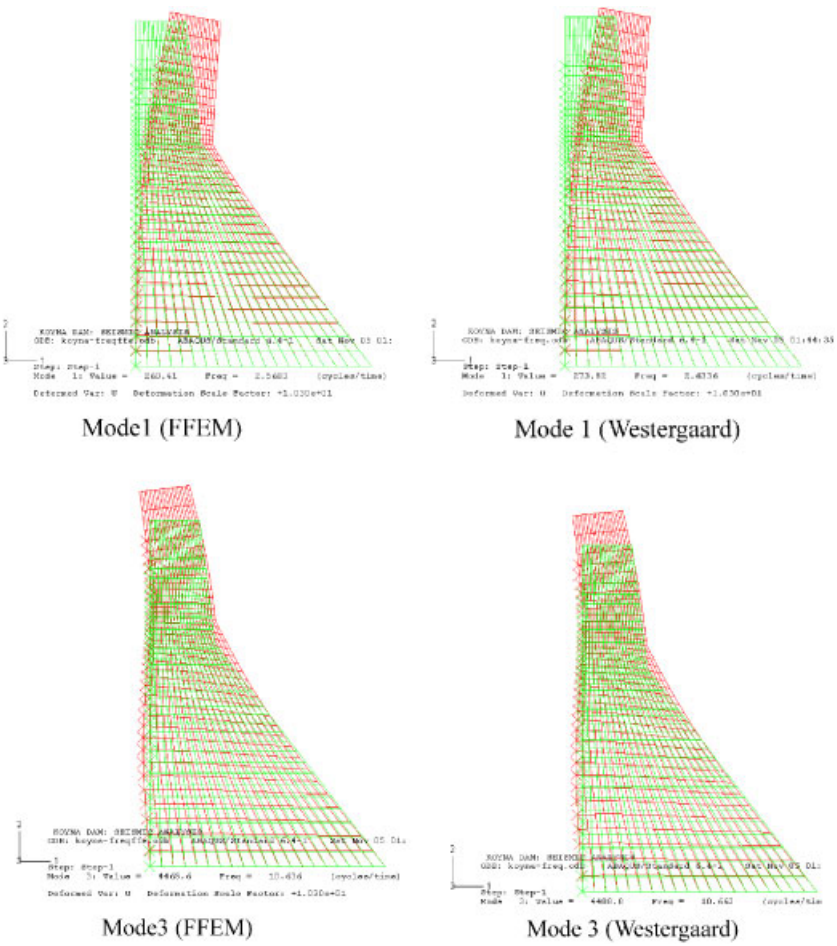

Figure 11. Predicted mode shapes of dam with full reservoir.

Table VI. Natural frequency (Hz) results for dam with full reservoir.

Mode	Westergaard	FFEM	FEM (200 m)	FEM (400 m)	FEM (800 m)
1	2.63	2.57	2.70	2.66	2.57
2	6.63	6.57	6.51	6.06	5.78
3	10.67	10.64	10.85	10.72	10.77
4	12.69	12.48	13.24	12.27	11.98

are perhaps more representative. ABAQUS does not seem to have an element that is based on potential flow, but its results using acoustic elements can be brought closer to the FFE results by increasing the bulk modulus of water to simulate incompressible fluid. However, the much

DOI: 10.1002/nme

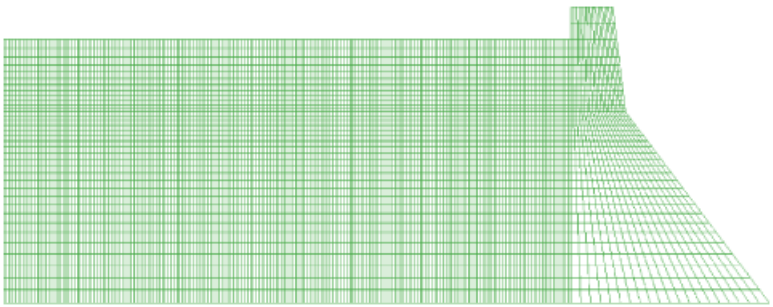

Figure 12. FE model with a truncated boundary (200 m) for the reservoir.

increased wavelength of the fluid motion means that a much larger fluid domain would be required to provide accurate solutions.

4. CONCLUSION

The FFEM has been successfully extended to the analysis of added-mass-type problems, including both axisymmetric and 2-D cases, with an infinite fluid domain. The use of a global interpolating function allows the infinite number of nodal pressures of the fractal finite elements representing the fluid to be condensed into a finite set of generalized coordinates by means of the fractal transformation technique. No new element formulations are involved for this method. The FFE solutions, which involve much fewer DOF in its computation, compare favourably with those reported in the literature. However, for compressible fluids that cannot be adequately modelled by the Laplace equation, the FFEM would significantly overestimate the added mass.

ACKNOWLEDGEMENTS

This research is supported by the Hong Kong Research Grants Council (Project no. CityU1047/00E) and the Hong Kong University through the Small Project Fund (2006-2007).

REFERENCES

1. Zienkiewicz C, Taylor RL. *The Finite Element Method* (5th edn). McGraw-Hill: London, 2000.
2. Junger MC, Mass C. Vibration of elastic shells in a fluid medium and the associated radiation of sound. *Journal of Applied Mechanics* 1952; **3**:439–444.
3. Bleich HH, Baron ML. Free and forced vibration of an infinitely long cylindrical shell in an infinite acoustic medium. *Journal of Applied Mechanics* 1954; **21**(3):167–177.
4. Hayek S. Vibration of a spherical shell in an acoustic medium. *The Journal of the Acoustical Society of America* 1966; **40**(2):342–348.
5. Nicolas-Vullierme B, Blumstein BD. Study of harmonic vibrations of fluid–structure coupled systems of revolution by means of the Bettess–Zienkiewicz mapped infinite element. In *International Conference on Numerical Methods for Transient and Coupled Problems*, Office National d'Etudes et de Recherches Aerospatiales (O.N.E.R.A), Chatillon, France, 1984; 887–902.
6. Nicolas-Vullierme B, Ohayon R. Fluid–structure interaction for bounded and infinite medium vibration problems. *Some Recent Advances at O.N.E.R.A*, Office National d'Etudes et de Recherches Aerospatiales (O.N.E.R.A), Chatillon, France, 1984; 243–253.

DOI: 10.1002/nme

7. Orsero P, Armand J-L. A numerical determination of the entrained water in ship vibrations. *International Journal for Numerical Methods in Engineering* 1978; **13**:35–48.
8. Armand J-L, Orsero P. A method for evaluating the hydrodynamic added mass in ship hull vibrations. *SNAME Transactions* 1979; **87**:99–120.
9. Ozsoysal R. A review of recent ship vibration papers. *The Shock and Vibration Digest* 2004; **36**:206–214.
10. Faltinsen OM. Hydroelastic slamming. *Journal of Marine Science and Technology* 2000; **5**:49–65.
11. Holloway DS, Thomas GA, Davis MR. Added mass of whipping modes for ships at high Froude number by a free surface boundary element method coupled with strip theory. *ANZIAM Journal* 2004; **45**(E):C831–C844.
12. Leung AYT, Dai H, Fok SL, Su RKL. The fractal finite element method for unbounded problems. *International Journal for Numerical Methods in Engineering* 2004; **61**(7):990–1008.
13. Gerdes K, Demkowicz L. Solution of 3d-Laplace and Helmholtz equations in exterior domains using hp-infinite elements. *Computer Methods in Applied Mechanics and Engineering* 1996; **137**:239–273.
14. Hibbit, Karsson and Sorenson, Inc. *ABAQUS User's Manual, Version 6.1*. Hibbit, Karsson and Sorenson, Inc., Pawtucket, RI, U.S.A., 2000.
15. Xie JF, Fok SL, Leung AYT. A parametric study on the fractal finite element method for 2-D crack problems. *International Journal for Numerical Methods in Engineering* 2003; **58**:631–642.
16. Kucukarslan S. Dam–reservoir interaction for incompressible-unbounded fluid domains using an exact truncation boundary condition. *Sixteenth ASCE Engineering Mechanics Conference*, University of Washington, Seattle, 16–18 July 2003.
17. Westergaard HM. Water pressure on dams during earthquakes. *Transactions of the ASCE* 1933; **98**:418–472.

DOI: 10.1002/nme